






Possible role of toroidal moments and Dzyaloshinskii-Moriya interaction in the magnetoelectric effect of the hyperkagome compound $\text{Mn}_3\text{Al}_2\text{Ge}_3\text{O}_{12}$

Leili Tan,¹ Guoqing Ma,¹ Shuhan Zheng ^{1,*}, Meifeng Liu,^{1,2,†} Jiahua Min,¹ Junhu Zhang ³, Yao Li,^{1,3} Yunlong Xie,^{1,3} Zhen Ma ¹, Yongjun Zhang,¹ Lin Lin ⁴, Xiuzhang Wang,¹ Hong Li,¹ Shuai Dong,⁵ and Jun-Ming Liu ^{1,3}


¹Hubei Key Laboratory of Photoelectric Materials and Devices, School of Materials Science and Engineering, Hubei Normal University, Huangshi 435002, China

²College of Physics and Electronic Science, Hubei Normal University, Huangshi 435002, China

³Laboratory of Solid State Microstructures, Nanjing University, Nanjing 210093, China

⁴Department of Applied Physics, College of Science, Nanjing Forestry University, Nanjing 210037, China

⁵Key Laboratory of Quantum Materials and Devices of Ministry of Education, School of Physics, Southeast University, Nanjing 211189, China

 (Received 1 April 2024; revised 17 October 2024; accepted 20 November 2024; published 6 December 2024)

The magnetoelectric (ME) effects originating from exotic magnetic states provide opportunities to explore novel topics such as topology and intriguing excitation. Herein, we report the ME effect in a cubic garnet $\text{Mn}_3\text{Al}_2\text{Ge}_3\text{O}_{12}$ with comprehensive magnetic and ferroelectric measurements. Our results reveal the dominant ME coefficient α with magnetic field perpendicular to electric field, in which electric polarization along the [110] axis is the strongest. We also observed a transition of coefficient α from negative to positive value upon switching of magnetic field. It is suggested that the ME effect of $\text{Mn}_3\text{Al}_2\text{Ge}_3\text{O}_{12}$ originates from the combination of special hyperkagome lattice and 120° magnetic configuration, which leads to a $-3'$ magnetic point group. The microscopic mechanism of the ME effect is discussed from viewpoints of toroidal moments and inverse Dzyaloshinskii-Moriya interaction. This work provides a scenario for understanding ME effect and further exploring the exotic state of $\text{Mn}_3\text{Al}_2\text{Ge}_3\text{O}_{12}$ and other garnets.

DOI: [10.1103/PhysRevB.110.245116](https://doi.org/10.1103/PhysRevB.110.245116)

I. INTRODUCTION

The magnetoelectric (ME) effect has long been an intriguing topic in condensed-matter physics, which involves the coupling of multiple degrees of freedom such as charge, spin, orbit, and lattice [1–5]. The mutual control of magnetism and ferroelectricity is promising in applications of memory with ultralow-energy consumption, sensors, multifunction electronic devices, etc. [6]. It is well known that remarkable ME effect may be realized in materials with magnetically induced ferroelectricity, such as type-II multiferroics and linear ME materials. From the viewpoint of symmetry, the presence of ferroelectricity requires broken spatial-inversion symmetry. Based on different ways of symmetry breaking, varied ME effect and associated physics are discussed in different systems [7–10]. Better ferroelectric properties and stronger ME effect in materials with low lattice symmetry, such as polar magnets Ni_3TeO_6 [11] and $\text{Fe}_2\text{Mo}_3\text{O}_8$ [12,13], are expected. Conversely, it is challenging to achieve ferroelectricity in cubic lattices since electric polarization is not allowed in a highly symmetrical system. To generate ferroelectricity in a cubic system, special magnetic configurations are required, and other physics may emerge. For example, unusual electric polarization in $\text{TbMn}_3\text{Cr}_4\text{O}_{12}$ [14,15], caused by Mn^{3+} and Cr^{3+} sublattices, forms a topological Roman face. Additionally,

in linear ME material Cu_3TeO_6 [16–19], an emergent excitation called topological magnon is observed. It seems that cubic systems with broken inversion symmetry provide a playground for exploring physics associated with the ME effect, topology, or excitations.

To seek broken symmetry in a cubic lattice, one may look into the [111] axis, which is the threefold rotation axis. In $\text{TbMn}_3\text{Cr}_4\text{O}_{12}$, Mn^{3+} and Cr^{3+} form a collinear structure along the [111] axis [14], in which the combination of sublattices breaks spatial inversion symmetry and introduces ferroelectricity. In Cu_3TeO_6 , however, the combination of chiral lattice structure and collinear spin structure along the [111] axis develops a magnetic point group of $-3'$ [4,20], which permits a linear ME effect under a magnetic field. These examples provide ideas for searching unique magnetic structures that break spatial inversion symmetry. Besides, it is noted that triangular geometry may be allowed on the (111) plane of cubic lattices, which may offer interesting lattice frustration and topology [21,22].

Following this idea, it is noted that the garnet family ($\text{A}_3\text{B}_2\text{C}_3\text{O}_{12}$, in which A, B, and C can be divalent, trivalent, and tetravalent ions, respectively), could be a promising candidate [23–25]. These materials crystallize in a complex lattice with cubic structure and have been widely studied due to their promising properties in spintronic devices [26–29]. The well-known one was $\text{Y}_3\text{Fe}_5\text{O}_{12}$ [27,30], in which magnetic Fe^{3+} ions are located on the B site and C site. Recently, other members in this family with magnetic ions on the A site were also discussed. The triangular lattice constructed by A-site

*Contact author: shzheng@hbnu.edu.cn

†Contact author: lmfeng1107@hbnu.edu.cn

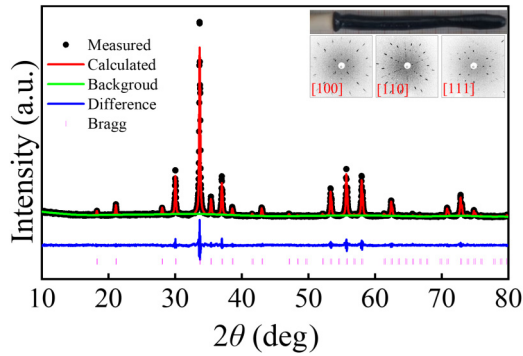


FIG. 1. Powder XRD patterns and Rietveld refinement of crushed $\text{Mn}_3\text{Al}_2\text{Ge}_3\text{O}_{12}$ single crystal at room temperature. The inset is the optical photograph of $\text{Mn}_3\text{Al}_2\text{Ge}_3\text{O}_{12}$ crystal grown via the optical floating-zone method and the Laue diffraction spots along the [100], [110], and [111] axes, respectively.

ions leads to strong geometrical frustration, allowing exotic magnetic ground states and excitations. For instance, a hidden order in the spin liquid state of $\text{Gd}_3\text{Ga}_5\text{O}_{12}$ [31] and a quantum spin state of Yb^{3+} in $\text{Yb}_3\text{Ga}_5\text{O}_{12}$ [32] have been reported. In 2022, ferroelectricity was reported in $\text{Mn}_3\text{Al}_2\text{Ge}_3\text{O}_{12}$ upon a magnetic field [33], and this was the first observation in the garnet family. It is believed that 120° antiferromagnetic structure in the (111) plane plays a crucial role in contributing the ME effect. However, the polycrystalline nature of the $\text{Mn}_3\text{Al}_2\text{Ge}_3\text{O}_{12}$ samples under study hindered the understanding of the ME effect. Certainly, a comprehensive investigation on single-crystal samples becomes urgent to reveal the ME effect and underlying mechanisms.

Inspired by these discussions, we have synthesized $\text{Mn}_3\text{Al}_2\text{Ge}_3\text{O}_{12}$ single crystals and systematically investigated its ME effect in this work. Our results reveal nonzero ME effects in both the $E//H$ and $E\perp H$ configurations. The signals of ME coefficients can be reversed by switching the magnetic field. Based on the analysis on symmetry and structure, one is able to unveil the microscopic mechanism of ferroelectricity and the ME effect in $\text{Mn}_3\text{Al}_2\text{Ge}_3\text{O}_{12}$.

II. EXPERIMENTAL DETAILS

The single crystals of $\text{Mn}_3\text{Al}_2\text{Ge}_3\text{O}_{12}$ were synthesized using the floating-zone method. Highly purified powders of MnO (99.95%), Al_2O_3 (99.99%), and GeO_2 (99.99%) were used as raw materials. The powder in a stoichiometric ratio was well ground and fired at 1200°C repeatedly to obtain pure-phase samples. Subsequently, the powder was pressed into a cylindrical shape using an isostatic pressing instrument and was fired at 1100°C for 12 h. The obtained rod was used for crystal growth using an optical floating-zone furnace (MF-2400, Cyberstar, France). High-quality $\text{Mn}_3\text{Al}_2\text{Ge}_3\text{O}_{12}$ crystals were successfully grown in air at a fast growth speed of 15 mm/h, agreeing with a recent report [34]. The growth in an Ar flow will lead to severe evaporation of GeO_2 . Besides, the floating zone became unstable when growing at a slow speed. The as-grown shiny crystal is rod shaped with a diameter of 7 mm and a length of 8 cm, as shown in the inset of Fig. 1.

The phase purity of as-grown crystals was checked using an x-ray diffractometer (Rigaku Smartlab SE) with $\text{Cu-K}\alpha$ radiation at room temperature. The diffraction spectrum was further analyzed using the Rietveld refinement method with the GSAS software package. The crystal quality and crystallographic orientation were checked using a back-reflection Laue detector (MWL 120, Multiwire Laboratories, Ltd.).

The magnetic susceptibility and heat capacity were measured using a physical property measurement system (PPMS Dynacool, Quantum Design). The electric polarization and ME effect were measured using a Keithley 6514A electrometer, while the detailed procedure of measurement process was described elsewhere [33].

III. EXPERIMENTAL RESULTS

A. X-ray diffraction and structural characterization

To characterize the lattice structure and crystal quality of $\text{Mn}_3\text{Al}_2\text{Ge}_3\text{O}_{12}$, we first carried out x-ray-diffraction (XRD) measurements using the crushed crystals. The Rietveld-refined pattern and lattice parameters are shown in Fig. 1 and Table I, respectively. The refinement result yields a cubic symmetry with space group $Ia-3d$, consistent with previous reports [33,35]. No diffraction from impurities is identified, and the fitted lattice parameters are $a = b = c = 11.8911(9)\text{\AA}$. The refined coordinates for O atoms slightly differ from previous work [33], which leads to a spatial deviation of $\sim 0.1\text{\AA}$. The difference should be attributed to the influence of grain boundaries and different synthesis conditions of polycrystalline samples and single crystals, as observed in many systems [36–38]. Besides, the inset of Fig. 1 presents the Laue diffraction spots of $\text{Mn}_3\text{Al}_2\text{Ge}_3\text{O}_{12}$ crystals along the [100], [110], and [111] axes, respectively. The clear spots suggest the high crystal quality. In addition, it is noted that the Laue spot pattern shows some fluctuations in different areas of the sample (not shown here), suggesting a presence of multiple grains of $\text{Mn}_3\text{Al}_2\text{Ge}_3\text{O}_{12}$ crystals. The typical size of grains is about $1 \sim 3\text{ mm}$. Then, the crystals were cut into slices with faces normal to the [100], [110], and [111] directions for characterizations. Each slice was cut and checked carefully using the Laue detector to ensure the slice was a single-grained sample.

B. Magnetization and heat capacity

Figure 2(a) presents the temperature dependence of magnetic susceptibility $\chi(T)$ with measuring magnetic field $\mu_0 H = 0.1\text{ T}$. The $\chi(T)$ curves measured with H applied along the [100], [110], and [111] axes exhibit a typical antiferromagnetic (AFM) behavior established at $T_N \sim 6.8\text{ K}$. The magnetic susceptibility shows similar magnitudes along all directions, suggesting a weak magnetic anisotropy of $\text{Mn}_3\text{Al}_2\text{Ge}_3\text{O}_{12}$. The AFM transition is further confirmed by heat-capacity measurements, as shown in Fig. 2(b). A λ -shaped peak is observed at $\sim 6.8\text{ K}$, in agreement with that determined from the $\chi(T)$ curves, and no other anomaly is observed. We also checked the heat capacity under a magnetic field of 9 T along the [111] direction. The peak slightly shifts towards lower temperature and its magnitude slightly decreases, suggesting a suppression of AFM order.

TABLE I. The atom coordinates (x, y, z), temperature factors (U_{iso}), and lattice parameters (a, b, c) of $\text{Mn}_3\text{Al}_2\text{Ge}_3\text{O}_{12}$ determined from x-ray-diffraction data using crushed crystals at room temperature. χ^2 , R_{wp} , and R_{p} are refinement factors.

Atom (site)	x	y	z	Occ.	U_{iso}
O (96h)	0.0278(5)	0.0499(6)	0.6463(5)	1	0.0205(0)
Mn (24c)	0	0.25	0.125	1	0.0176(3)
Al (16a)	0	0	0	1	0.0264(0)
Ge (24d)	0.375	0	0.25	1	0.0277(1)
Space group: $Ia\bar{3}d$, $a = b = c = 11.8911(9)\text{\AA}$, $\chi^2 = 1.952$, $R_{\text{wp}} = 7.33\%$, $R_{\text{p}} = 5.86\%$					

Such behavior is common in AFM systems with 3D structures [39–41]. Besides, the weak response of heat capacity to H implies a stable AFM configuration of $\text{Mn}_3\text{Al}_2\text{Ge}_3\text{O}_{12}$.

For some quantitative analysis of magnetic state and anisotropy, we replot the inverse susceptibility $1/\chi(T)$ in Fig. 2(c). The Curie-Weiss fitting in temperature range from 200 to 300 K gives the Curie-Weiss temperatures as $\theta_{\text{CW}-[100]} \sim -10.66$ K, $\theta_{\text{CW}-[110]} \sim -20$ K, and $\theta_{\text{CW}-[111]} \sim -16.78$ K, respectively. The negative θ_{CW} values confirm the dominant AFM interaction of $\text{Mn}_3\text{Al}_2\text{Ge}_3\text{O}_{12}$. The frustration factors $f = |\theta_{\text{CW}}|/T_{\text{N}}$ are less than 3.0 for all directions, suggesting a weak magnetic frustration of $\text{Mn}_3\text{Al}_2\text{Ge}_3\text{O}_{12}$. The obtained effective moments are $\mu_{[100]} \sim 5.80 \mu_{\text{B}}/\text{Mn}^{2+}$, $\mu_{[110]} \sim 5.90 \mu_{\text{B}}/\text{Mn}^{2+}$, and $\mu_{[111]} \sim 5.86 \mu_{\text{B}}/\text{Mn}^{2+}$, respectively, in agreement with theoretical prediction of the Mn^{2+} moment with high spin configuration ($S = 5/2$, $\mu_{\text{eff}} = 5.92 \mu_{\text{B}}/\text{Mn}^{2+}$).

Based on the heat-capacity data, we can discuss the contribution from the magnetization or magnetic ordering. The magnetic heat capacity C_{M} is obtained by subtracting the lattice contribution from the total heat capacity, assuming that those garnets have similar lattice contribution. The lattice heat capacity of $\text{Mn}_3\text{Al}_2\text{Ge}_3\text{O}_{12}$ is calculated using the Einstein

equation, considering three modes [42],

$$C_{\text{lat}}(T) = \sum_{i=1}^3 f_{\text{Ei}} \times 3nR \left(\frac{\theta_{\text{Ei}}}{T} \right)^2 \frac{\exp(\theta_{\text{Ei}})}{[\exp(\frac{\theta_{\text{Ei}}}{T}) - 1]^2}, \quad (1)$$

where θ_{Ei} and f_{Ei} represent, respectively, the Einstein temperature and corresponding fraction; n is the number of atoms per unit; and R is the ideal gas constant. The lattice-heat capacity via the fitting gives rise to parameters $\theta_{\text{E1}} = 139$ K, $f_{\text{E1}} = 0.12$; $\theta_{\text{E2}} = 338$ K, $f_{\text{E2}} = 0.38$; and $\theta_{\text{E3}} = 845$ K, $f_{\text{E3}} = 0.5$. Figure 3(a) shows the fitted lattice-heat capacity and measured heat capacity. It is seen that two curves coincide above 30 K. The subtracted magnetic-heat capacity is shown in Fig. 3(b), and magnetic entropy of $\text{Mn}_3\text{Al}_2\text{Ge}_3\text{O}_{12}$ is calculated with the following equation:

$$S_{\text{mag}}(T) = \int \frac{C_{\text{M}} dT}{T}. \quad (2)$$

The calculated magnetic entropy saturates at ~ 37.2 J/mol K above 30 K, which is smaller than the theoretical prediction of high spin state ($3R \ln 6 = 44.69$ J/mol K). The difference may originate from the residual entropy at low temperatures (below 2 K). It is noted that the contribution of short-range orders to the magnetic entropy

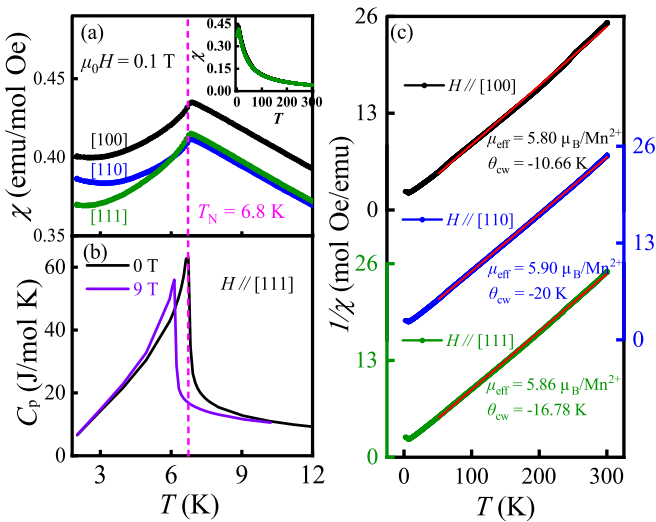


FIG. 2. (a) Temperature-dependent magnetic susceptibility $\chi(T)$ of $\text{Mn}_3\text{Al}_2\text{Ge}_3\text{O}_{12}$ along [100], [110], and [001] directions around T_{N} . The inset shows the $\chi(T)$ curves between 2 and 300 K. (b) Temperature-dependent heat capacity measured under zero field and 9 T along the [111] axis. (c) The Curie-Weiss fitting of inverse susceptibility $1/\chi(T)$.

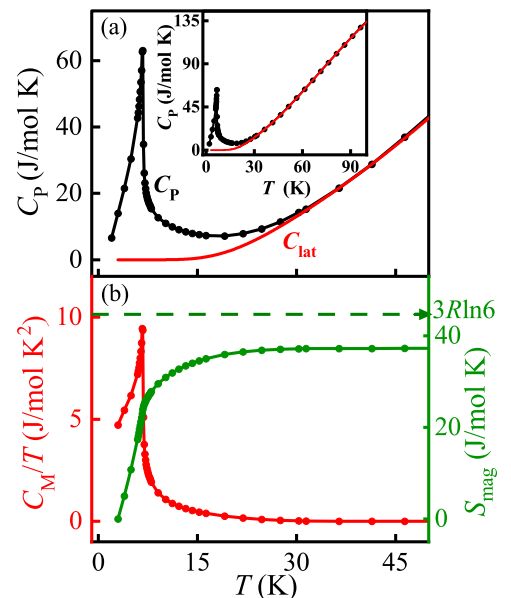


FIG. 3. (a) Fitting of lattice-heat capacity using the Einstein model. (b) Calculated magnetic-heat capacity and magnetic entropy of $\text{Mn}_3\text{Al}_2\text{Ge}_3\text{O}_{12}$.

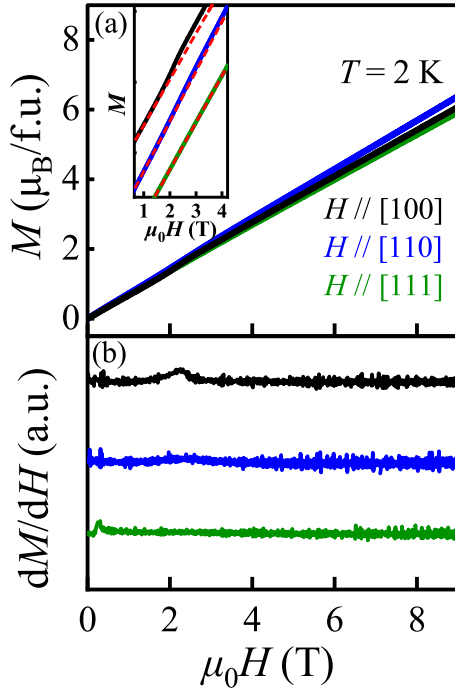


FIG. 4. (a) The dependence of magnetization on magnetic field $M(H)$ of $\text{Mn}_3\text{Al}_2\text{Ge}_3\text{O}_{12}$ at $T = 2$ K. (b) The derivative of $M(H)$ curves of $\text{Mn}_3\text{Al}_2\text{Ge}_3\text{O}_{12}$. The curves are vertically shifted for clarity.

above T_N is only $\sim 20\%$, which is much smaller than those AFM systems with high frustration [43,44]. This result further confirms the weak magnetically frustrated state with $\text{Mn}_3\text{Al}_2\text{Ge}_3\text{O}_{12}$.

Subsequently, we measured the magnetization as a function of H along the [100], [110], and [111] directions at $T = 2$ K, as shown in Fig. 4(a). The magnetization varies almost linearly with H along all three directions, and these curves show small differences, suggesting small magnetic anisotropy directly. The magnetization reaches $6 \mu_B/\text{f.u.}$ (formula units) under $\mu_0H = 9$ T, suggesting the significant spin rotation, consistent with scenario of weak interaction in $\text{Mn}_3\text{Al}_2\text{Ge}_3\text{O}_{12}$. It is noted that the $M(H)$ curve with H along the [100] direction exhibits a weak nonlinear behavior under low H . To clarify the possible H -induced transition, we plot the derivative of $M(H)$ curves in Fig. 4(b). A clear peak is observed at $\mu_0H_C \sim 2.3$ T for $H//[100]$. The result agrees with previous reports, corresponding to the rotation of Mn^{2+} spin plane from the (111) plane till the critical field H_C [45,46]. The spin rotation will significantly affect the ME effect in linear ME systems [11,47,48], and it is valuable to check this issue in the following measurements.

C. Ferroelectricity and ME effect

To characterize the ferroelectricity and ME effect, we first carried out pyroelectric measurements. Given the cubic structure ($a = b = c$) of $\text{Mn}_3\text{Al}_2\text{Ge}_3\text{O}_{12}$, the pyroelectric current I was measured along the [100], [110], and [111] axes, respectively. For each case, magnetic field ($\mu_0H = 0, 3, 6, 9$ T) was applied in parallel or perpendicular to the electric field. Subsequently, the electric polarization P was obtained

by integrating I over time and then dividing it by electrode area. The P - and pyroelectric current density J as functions of T are summarized in Fig. 5.

These results reveal an intriguing ME effect of $\text{Mn}_3\text{Al}_2\text{Ge}_3\text{O}_{12}$, with almost all ME coefficients appearing to be nonzero. For all cases, no current signal is observed with zero magnetic field. With increasing H , an increasing sharp current peak around T_N is observed, showing the emergence of ferroelectricity. The ME effect is approximately one order of magnitude stronger for $H \perp E$ configuration than for $E \parallel H$ configuration. Besides, the electric polarization exhibits moderate anisotropy. For $H \perp E$ configuration, the largest P appears along the [110] axis, which reaches $\sim 2.8 \mu\text{C}/\text{m}^2$ with $\mu_0H = 9$ T at $T = 2$ K and corresponds to ME coefficient $\alpha = \Delta P/\Delta H \sim 0.4$ ps/m. The $P_{[100]}$ and $P_{[111]}$ reaches ~ 1.5 and $\sim 2 \mu\text{C}/\text{m}^2$ with $\mu_0H = 9$ T, corresponding to $\alpha \sim 0.2$ and $\alpha \sim 0.3$ ps/m, respectively. For the $E \parallel H$ configuration, the integrated P is typically less than $0.5 \mu\text{C}/\text{m}^2$.

Subsequently, the response of P to H was investigated in the $H \perp E$ configuration at $T = 2$ K, as presented in Fig. 6. Along each of these directions, a current peak is observed around zero H and the current stabilizes under high H with an opposite signal. Such behavior is similar for polycrystalline samples, as reported previously [33]. It is noted that the fluctuation of temperature during the H sweeping process is less than 0.01 K, ruling out the possibility of magnetocaloric effect. Besides, for $E//[110]$, an anomaly is observed at ~ 2.3 T. This anomaly should correspond to a magnetic field-induced transition, as revealed in the $M(H)$ curves with H applied along the [100] axis. Based on the H -dependent current signal, one can obtain $P(H)$ curves, as shown in Figs. 6(d)–6(f). With increasing H , the polarization becomes negative at first, then undergoes a transition from negative to positive value under high H . The polarization reaches $P_{[100]} \sim 1.2 \mu\text{C}/\text{m}^2$, $P_{[110]} \sim 2.8 \mu\text{C}/\text{m}^2$, and $P_{[111]} \sim 1.9 \mu\text{C}/\text{m}^2$ with $\mu_0H = 9$ T, which is consistent with the pyroelectric results.

Then, we focus on the low- H region, in which the transition from negative P to a positive one occurs. In the previous measurements shown in Fig. 6, the poling magnetic field was determined to be 9 T, which was used as the starting point of the measurements. It would be interesting to see if the polarization can be reversed by a small poling magnetic field μ_0H_{poling} . To clarify this issue, we redid the H scanning measurements between -3 and 3 T with $\mu_0H_{\text{poling}} = 0.5, 0.7, 1$ T, as shown in Figs. 7(a)–7(d). The H -switching consequence is marked with arrows. These measurements yield the same results, and the $P(H)$ curves coincide with the data shown in Fig. 6(e). We further verified this result by carrying out the measurement in a periodic magnetic field, as shown in Figs. 7(e) and 7(f). The shape of the $P(H)$ curve is persistent and no hysteresis is observed. These results suggest a switching sign of ME coefficient α rather than a simple reversal of electric polarization.

It is noted that Mn^{2+} spins rotate significantly with H , as proved in the $M(H)$ measurement. The magnetic symmetry may vary, which leads to the sign reversal of α . Besides, the sign reversal of α was reported in Cr_2O_3 along the [111] axis, among other linear ME materials, when temperature decreased [49,50]. Such event is understood in terms of spin fluctuations at high temperatures and orbital contribution at

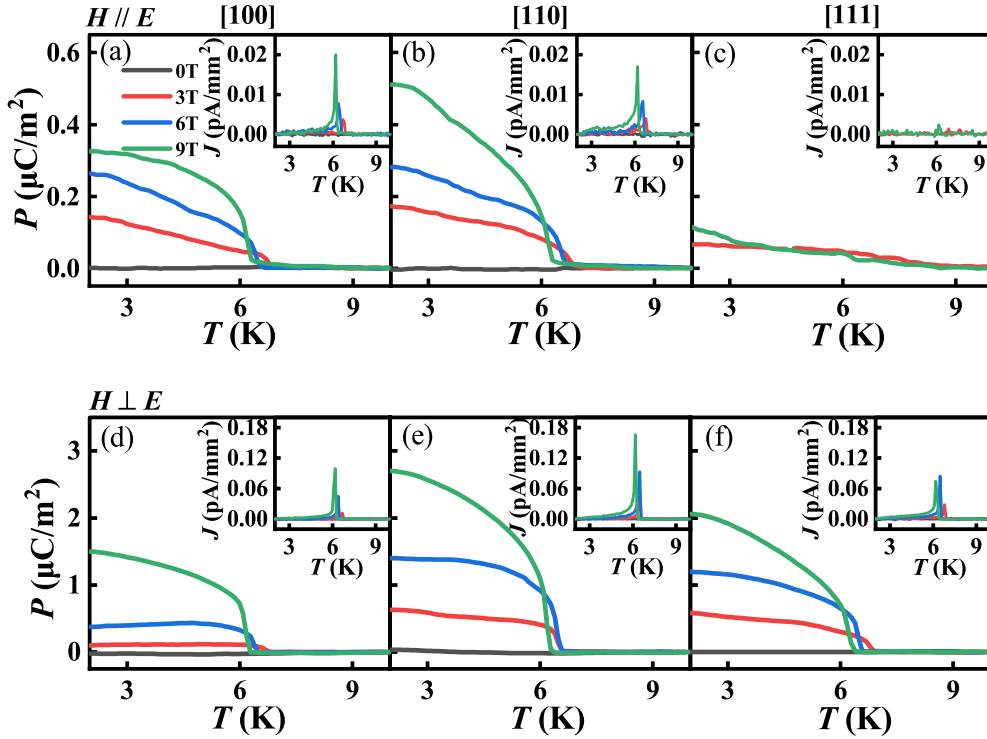


FIG. 5. Temperature-dependent electric polarization $P(T)$ along the [100], [110], and [111] axes with configuration (a)–(c) $H \parallel E$ and (d)–(f) $H \perp E$. The inset is temperature-dependent pyroelectric current density $J(T)$.

low temperatures. The antiferromagnetic domains are also believed to influence the sign of α , as well recognized in Cr_2O_3 and LiCoPO_4 [51–54]. In $\text{Mn}_3\text{Al}_2\text{Ge}_3\text{O}_{12}$, the influence of orbital magnetization should be negligible for Mn^{2+} ($L = 0$). To clarify the influence of possible variations in magnetic symmetry and AFM domains, neutron experiments under H are required, beyond the scope of this work but deserving future study.

IV. DISCUSSION OF ME MECHANISM

Subsequently, we discuss the ME effect observed in $\text{Mn}_3\text{Al}_2\text{Ge}_3\text{O}_{12}$. It is well known that the specific combination

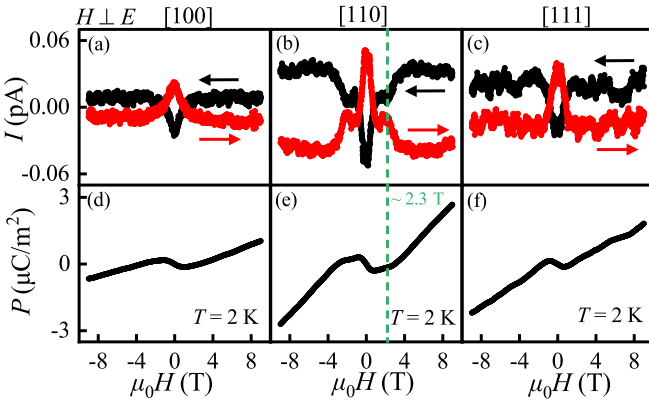


FIG. 6. Evolution of (a)–(c) electric current I ; and (d)–(f) electric polarization P with magnetic field H between 9 and 9 T. E is applied along the [100], [110], and [111] axes, while H is applied perpendicular to E . The black arrow and red arrow represent different H sweeping processes.

of lattice structure and magnetic configuration will lead to a linear ME effect in low-energy excited state. This scenario is used to predict ME effect in various systems [55,56]. In $\text{Mn}_3\text{Al}_2\text{Ge}_3\text{O}_{12}$, it is obvious that the magnetic structure owns the threefold rotational symmetry with respect to the [111] axis. Considering the centrosymmetric nature of magnetic structure, the magnetic point group of $\text{Mn}_3\text{Al}_2\text{Ge}_3\text{O}_{12}$ should be described as $-3'$, which allows nonzero ME coefficients $\alpha_{11} = \alpha_{22} = \alpha_{33}$, $\alpha_{12} = \alpha_{23} = \alpha_{31}$, and $\alpha_{13} = \alpha_{21} = \alpha_{32}$, as well discussed for another cubic ME system Cu_3TeO_6 [18]. Therefore, all nine coefficients can be nonzero, which agrees with our pyroelectric results.

In $\text{Mn}_3\text{Al}_2\text{Ge}_3\text{O}_{12}$, it is also obvious that the off-diagonal coefficients dominate the ME coupling, and thus negative coefficients can be observed. It is noteworthy that the Mn^{2+} moments may rotate significantly, as driven by H , leading to magnetization as large as $\sim 6 \mu_B/\text{f.u.}$ It is thus suggested that spin rotation can be a remarkable factor which likely results in variation of the magnetic point group and nonlinear ME behavior.

Subsequently, we focus on the microscopic mechanism of ME effect in $\text{Mn}_3\text{Al}_2\text{Ge}_3\text{O}_{12}$. Generally speaking, the ME effect in linear ME materials can be attributed to (i) exchange striction, (ii) spin dependent $p-d$ orbital hybridization, and (iii) inverse Dzyaloshinskii-Moriya (DM) interaction [2,57]. The possibility that the exchange striction works here as the dominant one is low, which is usually observed in systems with collinear magnetic structure. The contribution from the spin-dependent $p-d$ orbital hybridization should also be negligible due to the symmetrical environment of Mn ions.

In this work, we discuss the observed ME effect based on the scenario of inverse Dzyaloshinskii-Moriya interaction.

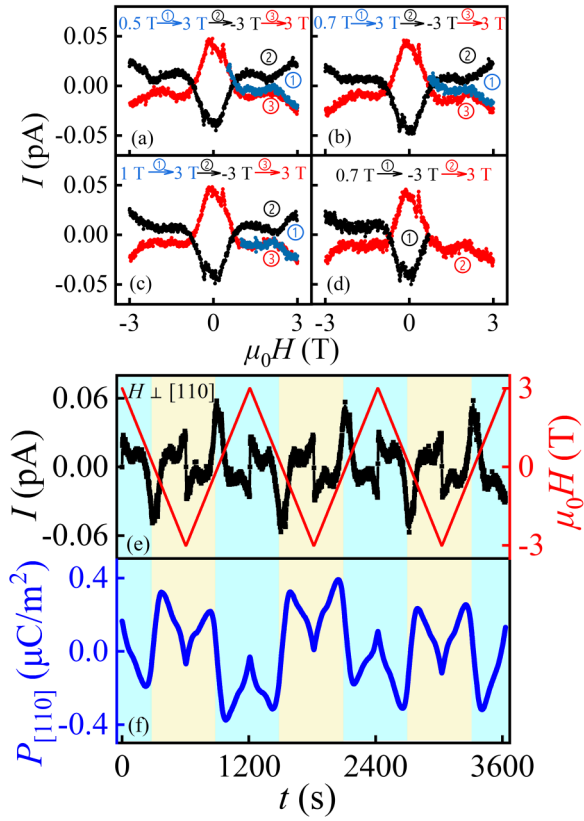


FIG. 7. (a)–(d) The H -dependent I with different poling and H scanning processes. (e), (f) Temporal evolution of electric current I and electric polarization P with a periodic magnetic field between -3 and 3 T, the blue and yellow areas denote area with $H > 0$ and $H < 0$, respectively.

The inverse DM interaction is also called flexomagnetolectric effect, which has been well explored in type-II multiferroic, both theoretically and experimentally [58–61]. Based on this effect, the as-generated electric dipole is $p \sim e_{ij} \times (S_i \times S_j)$, where S_i , S_j , and e_{ij} are adjacent spins and the direction vector between them. To clarify the flexomagnetolectric effect in $\text{Mn}_3\text{Al}_2\text{Ge}_3\text{O}_{12}$, a comprehensive analysis of lattice structure and magnetic structure is required. As has been well described in other garnets $\text{Gd}_3\text{Ga}_5\text{O}_{12}$ and $\text{Yb}_3\text{Ga}_5\text{O}_{12}$, the A-site ions form two interpenetrating

networks of opposite chirality, as shown in Fig. 8(a). Each network is constructed with corner-shared triangles. The moments of Mn^{2+} array along the $[11\bar{2}]$, $[\bar{2}11]$, and $[1\bar{2}1]$ axes or their opposite directions, forming a 120° structure [62,63]. Focusing on each Mn triangle, without external H , the induced p vectors form an equilateral triangle when the triangle lies in the (111) plane, leading to zero net polarization, as shown in Fig. 8(b). When the triangle deviates from the (111) plane, a nonzero polarization is expected. However, considering the symmetric structure of $\text{Mn}_3\text{Al}_2\text{Ge}_3\text{O}_{12}$, the polarization generated in different Mn triangles will cancel out and the net polarization should be zero. By applying a magnetic field, the spins rotate and the p vectors no longer cancel out, leading to a net P perpendicular to the magnetic field.

Besides the inverse DM interaction mechanism, the ME effect can also be discussed in the scenario of toroidal magnetic moment. As shown in Fig. 9(a), the corner-shared Mn triangles form the 10-spin-loop structure units. The local x axis can be identified as $\langle 100 \rangle$; y and z axes can be identified as $\langle 110 \rangle$. Considering the cubic symmetry, there are 12 possible orientations of these spin loops. In terms of the toroidal moment scenario, an electric polarization can be induced by a finite toroidal moment t , described by $P \sim -t \times H$ [64,65]. For $\text{Mn}_3\text{Al}_2\text{Ge}_3\text{O}_{12}$, the presence of vortexlike and antivortex-like structure should be equal in probability, if no poling field is applied, which leads to zero toroidal moment ($t \propto \sum_i r_i \times S_i$) in the statistical sense. However, upon a ME poling process, a finite toroidal moment may be generated ($+t$ for $+E_p$ and $-t$ for $-E_p$, where E_p is the poling electric field), as seen from the coupling term $t \cdot (E \times H)$.

It is noted that this scenario does not require a perfect vortex structure and the existence of xy component of the spin loop is sufficient to develop a finite toroidal moment. To check the validity of the scenario, we performed measurements on the H dependence of polarization P under two different ME poling processes ($+E_p/+H$ and $-E_p/+H$), as shown in Fig. 9(d). The $P(H)$ data are indeed reversed by reversing E_p , as predicted by this toroidal moment scenario, where the E_p reversal leads to the reversal of t . It is seen that the observed results agree with the toroidal scenario.

It should be mentioned that the two scenarios (mechanisms) discussed above are somehow equivalent. In the former

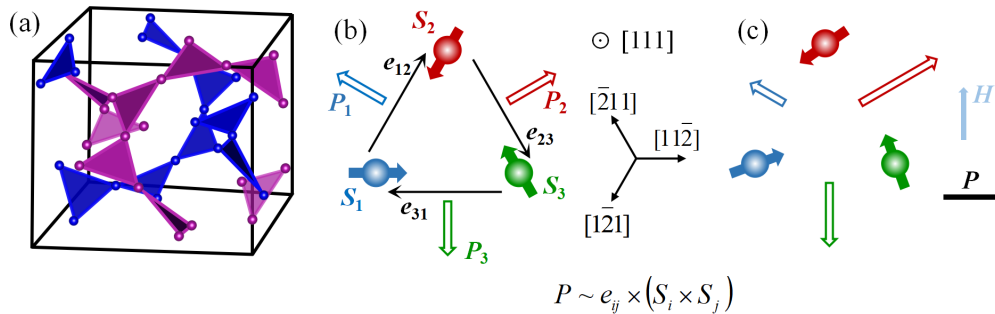


FIG. 8. (a) Two interpenetrating networks of corner-sharing triangles formed by Mn^{2+} ions. (b), (c) An illustration of microscopic mechanism for electric polarization P of $\text{Mn}_3\text{Al}_2\text{Ge}_3\text{O}_{12}$ in terms of inverse Dzyaloshinskii-Moriya (DM) interaction. The blue, red, and green spheres and solid arrows represent the Mn^{2+} ions and spins in a Mn triangle; e_{ij} represents the orientation vectors between two nearest-neighbor Mn ions.

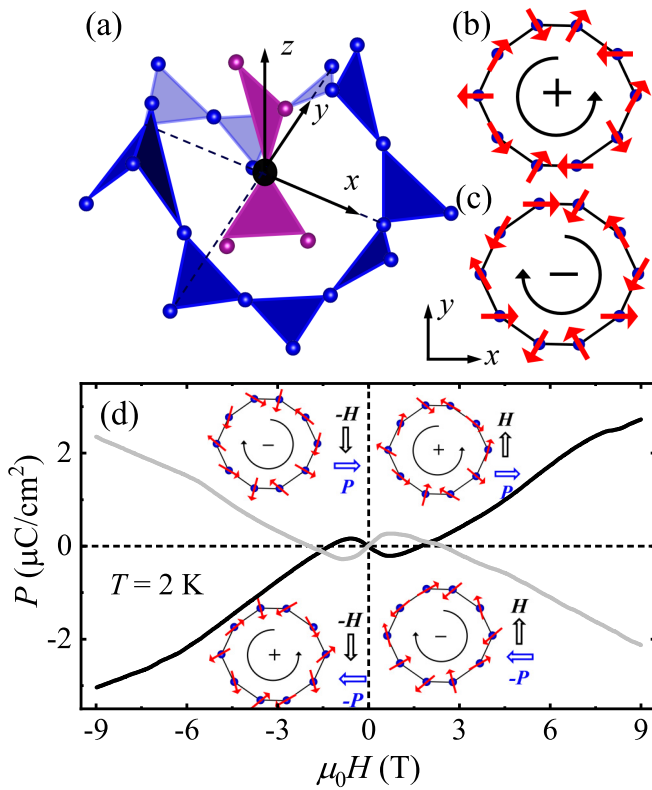


FIG. 9. (a) An illustration of Mn^{2+} loops constructed with 10 triangles. The (x, y, z) can be defined as $x \in \langle 100 \rangle$ and $y, z \in \langle 110 \rangle$. (b), (c) A representative illustration of toroidal magnetic moments of Mn^{2+} with + and - configuration projected on the xy plane. (d) H dependence of P measured under positive E_p (black line) and negative E_p (gray line), respectively. The illustrations present possible toroidal moments under H and the induced P .

case, the triangular spin will also lead to a finite toroidal moment t . In the latter case, P is also basically induced with the rotating spins under H . Therefore, the micromechanism of toroidal scenario should also be attributed to the inverse

DM interaction. Since both scenarios arise from spin-orbit coupling, it is natural that the ME effect of $\text{Mn}_3\text{Al}_2\text{Ge}_3\text{O}_{12}$ is weak considering the zero orbital moment of Mn^{2+} . It is noted that the ME coefficient of $\text{Mn}_3\text{Al}_2\text{Ge}_3\text{O}_{12}$ is quite close to $\text{Ni}_{1-x}\text{Mn}_x\text{TiO}_3$ [66]. Compound $\text{Ni}_{1-x}\text{Mn}_x\text{TiO}_3$ is an XY spin-glass system and the toroidal scenario is believed to be responsible for ME effect. The similar ME coefficients of $\text{Mn}_3\text{Al}_2\text{Ge}_3\text{O}_{12}$ and $\text{Ni}_{1-x}\text{Mn}_x\text{TiO}_3$ will support the reliability of the above discussion. Due to the complex structure and relatively small ME coefficient of $\text{Mn}_3\text{Al}_2\text{Ge}_3\text{O}_{12}$, it will be challenging to give a reliable ME coefficient in the quantitative sense.

V. CONCLUSION

In summary, we have systematically investigated the magnetism and ME effect of $\text{Mn}_3\text{Al}_2\text{Ge}_3\text{O}_{12}$. The ME effect can be realized with $E//H$ and $H \perp E$, suggesting nine nonzero ME coefficients. The ME effect is consistent with magnetic point group $-3'$. It is found that the off-diagonal coefficients dominate the ME effect and these coefficients can be reversed by switching magnetic field. The ME effect is explained in the views of inverse DM interaction and toroidal magnetic moment. This work will contribute to the understanding of ME effect in cubic systems and the exploration of the ME effect and excitation in the future.

ACKNOWLEDGMENTS

This work was supported by the National Natural Science Foundation of China (Grants No. 12274231, No. 12204160, No. 1230042123, No. 12074111, No. 52272108, and No. 12474113), Hubei Provincial Natural Science Foundation of China (Grant No. 2023AFA105), Innovation and Development Joint Fund of Huangshi (Grant No. 2022CFD040), and Young Teachers Research Grant Program of Hubei Normal University (Grant No. HS2021QN039). The Young Top-notch Talent Cultivation Program of Hubei Province.

- [1] S.-W. Cheong and M. Mostovoy, Multiferroics: A magnetic twist for ferroelectricity, *Nat. Mater.* **6**, 13 (2007).
- [2] Y. Tokura, S. Seki, and N. Nagaosa, Multiferroics of spin origin, *Rep. Prog. Phys.* **77**, 076501 (2014).
- [3] S. Dong, J.-M. Liu, S.-W. Cheong, and Z. Ren, Multiferroic materials and magnetoelectric physics: Symmetry, entanglement, excitation, and topology, *Adv. Phys.* **64**, 519 (2015).
- [4] N. A. Spaldin and R. Ramesh, Advances in magnetoelectric multiferroics, *Nat. Mater.* **18**, 203 (2019).
- [5] F. Liu, Y. Hao, J. Ni, Y. Zhao, D. Zhang, G. Fabbris, D. Haskel, S. Cheng, X. Xu, and L. Yin, Pressure-induced charge orders and their postulated coupling to magnetism in hexagonal multiferroic LuFe_2O_4 , *npj Quantum Mater.* **8**, 1 (2023).
- [6] V. Garcia and M. Bibes, Ferroelectric tunnel junctions for information storage and processing, *Nat. Commun.* **5**, 4289 (2014).
- [7] T. Kimura, T. Goto, H. Shintani, K. Ishizaka, T. Arima, and Y. Tokura, Magnetic control of ferroelectric polarization, *Nature(London)* **426**, 55 (2003).
- [8] J. Wang, J. Neaton, H. Zheng, V. Nagarajan, S. Ogale, B. Liu, D. Viehland, V. Vaithyanathan, D. Schlom, and U. Waghmare, Epitaxial BiFeO_3 multiferroic thin film heterostructures, *Science* **299**, 1719 (2003).
- [9] B. B. Van Aken, T. T. Palstra, A. Filippetti, and N. A. Spaldin, The origin of ferroelectricity in magnetoelectric YMnO_3 , *Nat. Mater.* **3**, 164 (2004).
- [10] S. Mitsuda, M. Mase, K. Prokes, H. Kitazawa, and H. Aruga Katori, Field-induced magnetic phase transitions in a triangular lattice antiferromagnet CuFeO_2 up to 14.5T, *J. Phys. Soc. Jpn.* **69**, 3513 (2000).
- [11] J. W. Kim, S. Artyukhin, E. D. Mun, M. Jaime, N. Harrison, A. Hansen, J. Yang, Y. S. Oh, D. Vanderbilt, and V. S. Zapf, Successive magnetic-field-induced transitions and colossal magnetoelectric effect in Ni_3TeO_6 , *Phys. Rev. Lett.* **115**, 137201 (2015).
- [12] T. Kurumaji, S. Ishiwata, and Y. Tokura, Doping-tunable ferrimagnetic phase with large linear magnetoelectric effect in a polar magnet $\text{Fe}_2\text{Mo}_3\text{O}_8$, *Phys. Rev. X* **5**, 031034 (2015).

- [13] Y. Wang, G. L. Pascut, B. Gao, T. A. Tyson, K. Haule, V. Kiryukhin, and S.-W. Cheong, Unveiling hidden ferrimagnetism and giant magnetoelectricity in polar magnet $\text{Fe}_2\text{Mo}_3\text{O}_8$, *Sci. Rep.* **5**, 12268 (2015).
- [14] Z. Wang, Y. Chai, and S. Dong, First-principles demonstration of Roman-surface topological multiferroicity, *Phys. Rev. B* **108**, L060407 (2023).
- [15] G. Liu, M. Pi, L. Zhou, Z. Liu, X. Shen, X. Ye, S. Qin, X. Mi, X. Chen, and L. Zhao, Physical realization of topological Roman surface by spin-induced ferroelectric polarization in cubic lattice, *Nat. Commun.* **13**, 2373 (2022).
- [16] W. Yao, C. Li, L. Wang, S. Xue, Y. Dan, K. Iida, K. Kamazawa, K. Li, C. Fang, and Y. Li, Topological spin excitations in a three-dimensional antiferromagnet, *Nat. Phys.* **14**, 1011 (2018).
- [17] S. Bao, J. Wang, W. Wang, Z. Cai, S. Li, Z. Ma, D. Wang, K. Ran, Z.-Y. Dong, and D. Abernathy, Discovery of coexisting Dirac and triply degenerate magnons in a three-dimensional antiferromagnet, *Nat. Commun.* **9**, 2591 (2018).
- [18] Y. Tang, L. Lin, G. Zhou, W. Zhai, L. Huang, J. Zhang, S. Zheng, M. Liu, Z. Yan, X. Jiang, X. Li, and J.-M. Liu, Realization of linear magnetoelectric effect in the Dirac magnon system Cu_3TeO_6 , *Phys. Rev. B* **107**, 214416 (2023).
- [19] V. Kisiček, D. Dominko, M. Čulo, Ž. Rapljenović, M. Kuveždić, M. Dragičević, H. Berger, X. Rocquefelte, M. Herak, and T. Ivek, Spin-reorientation-driven linear magnetoelectric effect in topological antiferromagnet Cu_3TeO_6 , *Phys. Rev. Lett.* **132**, 096701 (2024).
- [20] M. Herak, H. Berger, M. Prester, M. Miljak, I. Živković, O. Milat, D. Drobac, S. Popović, and O. Zaharko, Novel spin lattice in Cu_3TeO_6 : An antiferromagnetic order and domain dynamics, *J. Phys.: Condens. Matter* **17**, 7667 (2005).
- [21] M. Kang, S. Fang, L. Ye, H. C. Po, J. Denlinger, C. Jozwiak, A. Bostwick, E. Rotenberg, E. Kaxiras, and J. G. Checkelsky, Topological flat bands in frustrated kagome lattice CoSn , *Nat. Commun.* **11**, 4004 (2020).
- [22] Y. Hu, X. Wu, A. P. Schnyder, and M. Shi, Electronic landscape of kagome superconductors AV_3Sb_5 ($A = \text{K}, \text{Rb}, \text{Cs}$) from angle-resolved photoemission spectroscopy, *npj Quantum Mater.* **8**, 67 (2023).
- [23] S. Geller, Crystal chemistry of the garnets, *Zeitschrift für Kristallographie – Crystalline Materials* **125**, 1 (1967).
- [24] R. Watson and A. Freeman, Origin of effective fields in magnetic materials, *Phys. Rev.* **123**, 2027 (1961).
- [25] W. E. Courtney, Analysis and evaluation of a method of measuring the complex permittivity and permeability microwave insulators, *IEEE Trans. Microwave Theory Tech.* **18**, 476 (1970).
- [26] Ü. Özgür, Y. Alivov, and H. Morkoç, Microwave ferrites, Part I: Fundamental properties, *J. Mater. Sci.: Mater. Electron.* **20**, 789 (2009).
- [27] A. Serga, A. Chumak, and B. Hillebrands, YIG magnonics, *J. Phys. D: Appl. Phys.* **43**, 264002 (2010).
- [28] B. Heinrich, C. Burrowes, E. Montoya, B. Kardasz, E. Girt, Y.-Y. Song, Y. Sun, and M. Wu, Spin pumping at the magnetic insulator (YIG)/normal metal (Au) interfaces, *Phys. Rev. Lett.* **107**, 066604 (2011).
- [29] L. Cornelissen, J. Liu, R. Duine, J. B. Youssef, and B. Van Wees, Long-distance transport of magnon spin information in a magnetic insulator at room temperature, *Nat. Phys.* **11**, 1022 (2015).
- [30] D. Rodic, M. Mitric, R. Tellgren, H. Rundlof, and A. Kremenovic, True magnetic structure of the ferrimagnetic garnet $\text{Y}_3\text{Fe}_5\text{O}_{12}$ and magnetic moments of iron ions, *J. Magn. Magn. Mater.* **191**, 137 (1999).
- [31] J. A. Paddison, H. Jacobsen, O. A. Petrenko, M. T. Fernández-Díaz, P. P. Deen, and A. L. Goodwin, Hidden order in spin-liquid $\text{Gd}_3\text{Ga}_5\text{O}_{12}$, *Science* **350**, 179 (2015).
- [32] L. Ø. Sandberg, R. Edberg, I.-M. B. Bakke, K. S. Pedersen, M. C. Hatnean, G. Balakrishnan, L. Mangin-Thro, A. Wildes, B. Fåk, G. Ehlers, G. Sala, P. Henelius, K. Lefmann, and P. P. Deen, Emergent magnetic behavior in the frustrated $\text{Yb}_3\text{Ga}_5\text{O}_{12}$ garnet, *Phys. Rev. B* **104**, 064425 (2021).
- [33] J. Min, S. Zheng, J. Gong, X. Chen, F. Liu, Y. Xie, Y. Zhang, Z. Ma, M. Liu, and X. Wang, Magnetoelectric effect in garnet $\text{Mn}_3\text{Al}_2\text{Ge}_3\text{O}_{12}$, *Inorg. Chem.* **61**, 86 (2021).
- [34] M. Islam, M. Ciomaga Hatnean, G. Balakrishnan, and O. A. Petrenko, Frustrated magnet $\text{Mn}_3\text{Al}_2\text{Ge}_3\text{O}_{12}$ garnet: Crystal growth by the optical floating zone method, *cryst.* **13**, 397 (2023).
- [35] A. Gukasov, V. Plakhty, B. Dorner, S. Y. Kokovin, V. Syromyatnikov, O. Smirnov, and Y. P. Chernenkov, Inelastic neutron scattering study of spin waves in the garnet with a triangular magnetic structure, *J. Phys.: Condens. Matter* **11**, 2869 (1999).
- [36] J.-Q. Yan, S. Okamoto, Y. Wu, Q. Zheng, H. D. Zhou, H. B. Cao, and M. A. McGuire, Magnetic order in single crystals of $\text{Na}_3\text{Co}_2\text{SbO}_6$ with a honeycomb arrangement of $3d^7$ Co^{2+} ions, *Phys. Rev. Mater.* **3**, 074405 (2019).
- [37] L. Viciu, Q. Huang, E. Morosan, H. Zandbergen, N. Greenbaum, T. McQueen, and R. Cava, Structure and basic magnetic properties of the honeycomb lattice compounds $\text{Na}_2\text{Co}_2\text{TeO}_6$ and $\text{Na}_3\text{Co}_2\text{SbO}_6$, *J. Solid State Chem.* **180**, 1060 (2007).
- [38] G. Xiao, Z. Xia, W. Zhang, X. Yue, S. Huang, X. Zhang, F. Yang, Y. Song, M. Wei, and H. Deng, Crystal growth and the magnetic properties of $\text{Na}_2\text{Co}_2\text{TeO}_6$ with quasi-two-dimensional honeycomb lattice, *Cryst. Growth Des.* **19**, 2658 (2019).
- [39] M. Liu, L. Lin, Y. Zhang, S. Li, Q. Huang, V. O. Garlea, T. Zou, Y. Xie, Y. Wang, C. Lu, L. Yang, Z. Yan, X. Wang, S. Dong, and J.-M. Liu, Cycloidal magnetism driven ferroelectricity in double tungstate $\text{LiFe}(\text{WO}_4)_2$, *Phys. Rev. B* **95**, 195134 (2017).
- [40] X. Chen, S. Zheng, M. Liu, T. Zou, W. Wang, K. Nie, F. Liu, Y. Xie, M. Zeng, and X. Wang, Direct evidence for an intermediate multiferroic phase in $\text{LiCuFe}_2(\text{VO}_4)_3$, *Inorg. Chem.* **61**, 944 (2021).
- [41] Y. S. Tang, S. M. Wang, L. Lin, C. Li, S. H. Zheng, C. F. Li, J. H. Zhang, Z. B. Yan, X. P. Jiang, and J.-M. Liu, Collinear magnetic structure and multiferroicity in the polar magnet $\text{Co}_2\text{Mo}_3\text{O}_8$, *Phys. Rev. B* **100**, 134112 (2019).
- [42] Q. Cui, Q. Huang, J. A. Alonso, D. Sheptyakov, C. R. De la Cruz, M. T. Fernández-Díaz, N. N. Wang, Y. Q. Cai, D. Li, X. L. Dong, H. D. Zhou, and J.-G. Cheng, Complex antiferromagnetic order in the garnet $\text{Co}_3\text{Al}_2\text{Si}_3\text{O}_{12}$, *Phys. Rev. B* **101**, 144424 (2020).
- [43] R. Kumar and A. Sundaresan, Unveiling a hidden multiferroic state under magnetic fields in BaHoFeO_4 , *Phys. Rev. B* **107**, 184420 (2023).
- [44] S. Mishra, P. Yanda, F. Orlandi, P. Manuel, H.-J. Koo, M.-H. Whangbo, and A. Sundaresan, Contrasting magnetic and

- magnetoelectric properties of LuMWO_6 ($M = \text{Fe}$ and Cr): Role of spin frustration and noncollinear magnetic structure, *Phys. Rev. B* **108**, 014435 (2023).
- [45] Z. A. Kazei, N. P. Kolmakova, M. V. Levanidov, B. V. Mill, and V. I. Sokolov, Magnetoanisotropic properties of the exchange-noncollinear antiferromagnet $\text{Mn}_3\text{Al}_3\text{Ge}_3\text{O}_{12}$, *Sov. Phys. JETP* **65**, 1283 (1987).
- [46] A. M. Tikhonov, N. G. Pavlov, and O. G. Udalov, Nuclear magnetic resonance in noncollinear antiferromagnet $\text{Mn}_3\text{Al}_2\text{Ge}_3\text{O}_{12}$, *JETP Lett.* **96**, 517 (2012).
- [47] N. Mufti, G. Blake, M. Mostovoy, S. Riyadi, A. Nugroho, and T. T. Palstra, Magnetoelectric coupling in MnTiO_3 , *Phys. Rev. B* **83**, 104416 (2011).
- [48] Z. Yu, H. Ding, K. Zhai, C. Mu, A. Nie, J. Cong, J. Huang, H. Zhou, Q. Wang, and F. Wen, Crystal structure, spin flop transition, and magnetoelectric effect in the honeycomb-lattice frustrated Fe-doped $\text{Ni}_2\text{Mo}_3\text{O}_8$ antiferromagnets, *Phys. Rev. B* **109**, 024442 (2024).
- [49] I. E. Dzyaloshinskii, On the magneto-electrical effect in antiferromagnets, *Sov. Phys. JETP* **10**, 628 (1960).
- [50] D. N. Astrov, The magnetoelectric effect in antiferromagnetics, *Sov. Phys. JETP* **11**, 708 (1960).
- [51] E. Bousquet, E. Lelièvre-Berna, N. Qureshi, J.-R. Soh, N. A. Spaldin, A. Urru, X. H. Verbeek, and S. F. Weber, On the sign of the linear magnetoelectric coefficient in Cr_2O_3 , *J. Phys.: Condens. Matter* **36**, 155701 (2024).
- [52] P. Brown, J. Forsyth, and F. Tasset, A study of magnetoelectric domain formation in, *J. Phys.: Condens. Matter* **10**, 663 (1998).
- [53] E. Bousquet, N. A. Spaldin, and K. T. Delaney, Unexpectedly large electronic contribution to linear magnetoelectricity, *Phys. Rev. Lett.* **106**, 107202 (2011).
- [54] V. Kocsis, Y. Tokunaga, Y. Tokura, and Y. Taguchi, Switching of antiferromagnetic states in LiCoPO_4 as investigated via the magnetoelectric effect, *Phys. Rev. B* **104**, 054426 (2021).
- [55] S.-W. Cheong, SOS: Symmetry-operational similarity, *npj Quantum Mater.* **4**, 53 (2019).
- [56] J.-P. Rivera, A short review of the magnetoelectric effect and related experimental techniques on single phase (multi-) ferroics, *Eur. Phys. J. B.* **71**, 299 (2009).
- [57] M. Fiebig, T. Lottermoser, D. Meier, and M. Trassin, The evolution of multiferroics, *Nat. Rev. Mater.* **1**, 16046 (2016).
- [58] H. Katsura, N. Nagaosa, and A. V. Balatsky, Spin current and magnetoelectric effect in noncollinear magnets, *Phys. Rev. Lett.* **95**, 057205 (2005).
- [59] P. Bruno and V. K. Dugaev, Equilibrium spin currents and the magnetoelectric effect in magnetic nanostructures, *Phys. Rev. B* **72**, 241302(R) (2005).
- [60] M. Mostovoy, Ferroelectricity in spiral magnets, *Phys. Rev. Lett.* **96**, 067601 (2006).
- [61] I. S. Veshchunov, S. V. Mironov, W. Magrini, V. S. Stolyarov, A. N. Rossolenko, V. A. Skidanov, J.-B. Trebbia, A. I. Buzdin, P. Tamarat, and B. Lounis, Direct evidence of flexomagneto-electric effect revealed by single-molecule spectroscopy, *Phys. Rev. Lett.* **115**, 027601 (2015).
- [62] R. Plumier, Détermination par diffraction des neutrons de la structure antiferromagnétique du grenat $\text{Mn}_3\text{Al}_2\text{Ge}_3\text{O}_{12}$, *Solid State Commun.* **12**, 109 (1973).
- [63] W. Prandl, Rhombohedral magnetic structure in spessartite type garnets, *Phys. Status Solidi B* **55**, K159 (1973).
- [64] H. Schmid, On ferrotoroidics and electrotoroidic, magnetotoroidic and piezotoroidic effects, *Ferroelectrics* **252**, 41 (2001).
- [65] N. A. Spaldin, M. Fiebig, and M. Mostovoy, The toroidal moment in condensed-matter physics and its relation to the magnetoelectric effect, *J. Phys.: Condens. Matter* **20**, 434203 (2008).
- [66] Y. Yamaguchi, T. Nakano, Y. Nozue, and T. Kimura, Magneto-electric effect in an XY-like spin glass system $\text{Ni}_x\text{Mn}_{1-x}\text{TiO}_3$, *Phys. Rev. Lett.* **108**, 057203 (2012).